Geophys. J. Int. (2009) **178,** 488–502 doi: 10.1111/j.1365-246X.2009.04166.x

Active faults and induced seismicity in the Val d'Agri area (Southern Apennines, Italy)

L. Valoroso,[1] L. Improta,[2] L. Chiaraluce,[1] R. Di Stefano,[1] L. Ferranti,[3] A. Govoni[1,4] and C. Chiarabba[1]

[1] *Istituto Nazionale di Geofisica e Vulcanologia, Centro Nazionale Terremoti, Roma, Italy. E-mail: valoroso@ingv.it*
[2] *Istituto Nazionale di Geofisica e Vulcanologia, Sismologia e Tettonofisica, Roma, Italy*
[3] *Università degli Studi di Napoli "Federico II", Napoli, Italy*
[4] *Istituto Nazionale di Oceanografia e di Geofisica Sperimentale, Udine, Italy*

Accepted 2009 February 20. Received 2009 February 17; in original form 2008 June 20

SUMMARY

The NW–SE trending Val d'Agri extensional basin is one of the regions in Italy with the highest seismogenic potential. Field data do not univocally define which of the fault systems bordering the basin on the two opposite sides is accommodating the active deformation. In this study, we detect and locate, by using an automatic picking procedure, almost 2000 low-magnitude earthquakes ($-0.2 < M_L < 2.7$) recorded by a dense network during a 13-months-long seismic experiment. Events are mostly located along the southwestern flank of the basin. To the south, intense swarm-type microseismicity defines a major cluster ∼5 km wide from 1 to 5 km depth. To the west, a clear alignment of events, characterized by normal faulting kinematics, defines a NE-dipping normal fault between 1 and 6 km depth. The upward continuation of this structure, ∼5 km long, matches a mapped active normal fault recognized by field and palaeoseismological surveys.

A temporal correlation found between the intense swarm-type microseismicity and the water level changes in the nearby artificial Pertusillo lake suggests that this seismicity is reservoir-induced.

Key words: Earthquake interaction, forecasting, and prediction; Seismicity and tectonics; Fractures and faults.

1 INTRODUCTION

Quaternary crustal extension in the southern Apennines (Italy) has been accommodated by NW-trending high-angle normal faults (Fig. 1). Most of these faults show a south-westerly sense of extensional displacement and have mature morphologic and structural features, similar to a classical range-bounding faulting model (e.g. Basin & Range Province; Wallace 1984). However, coseismic faulting has occurred on NE-dipping structures, which do not have clear morphological expression at the surface (e.g. 1980 Irpinia *M* 6.9 normal-faulting earthquake, Pantosti & Valensise 1990).

Normal faults in the Apennines are superimposed onto compressive structures developed during Miocene–Early Pleistocene shortening (Patacca *et al.* 1990), which still remain the main features that modelled the landscape and the crustal structure (Pantosti & Valensise 1990; Menardi Noguera & Rea 2000; Mazzoli *et al.* 2000; Butler *et al.* 2004; Shiner *et al.* 2004). Consequently, in many cases, field data and subsurface seismic imaging do not have the resolution to identify the faults that accommodate the present-day extension and that are responsible for large destructive earthquakes (Mazzotti *et al.* 2000; Valensise & Pantosti 2001).

Difficulties in understanding the geometry of the major active faults is typified in the Val d'Agri basin, where the 1857 M7.0 earthquake is attributed to the eastern (Eastern Agri Fault System, EAFS in Fig. 2; Benedetti *et al.* 1998; Cello *et al.* 2003; Barchi *et al.* 2006) or, alternatively, to the western fault system (Monti della Maddalena Fault System, MMFS in Fig. 2; Maschio *et al.* 2005; Burrato & Valensise 2008).

In regions similar to the Val d'Agri basin, where active faults imaging is a difficult task, a dense seismic survey can be a powerful tool to image active faults with microseismicity data (Eberhart-Phillips & Michael 1993; Thurber *et al.* 2004; Waldhauser *et al.* 2004; Chiaraluce *et al.* 2007; among many others). The use of local networks allows for decreasing the magnitude threshold for earthquake detection and obtaining high-resolution hypocentral locations. This is a pre-requisite to accurately investigate the behaviour of the low-magnitude seismic activity and to unravel fault geometry at depth (Rigo *et al.* 1996; Hatzfeld *et al.* 2000; Bagh *et al.* 2007).

In this paper, we investigate the geometry and kinematics of the Val d'Agri normal fault systems by earthquake distribution. We use about 2000 low-magnitude microearthquakes, automatically

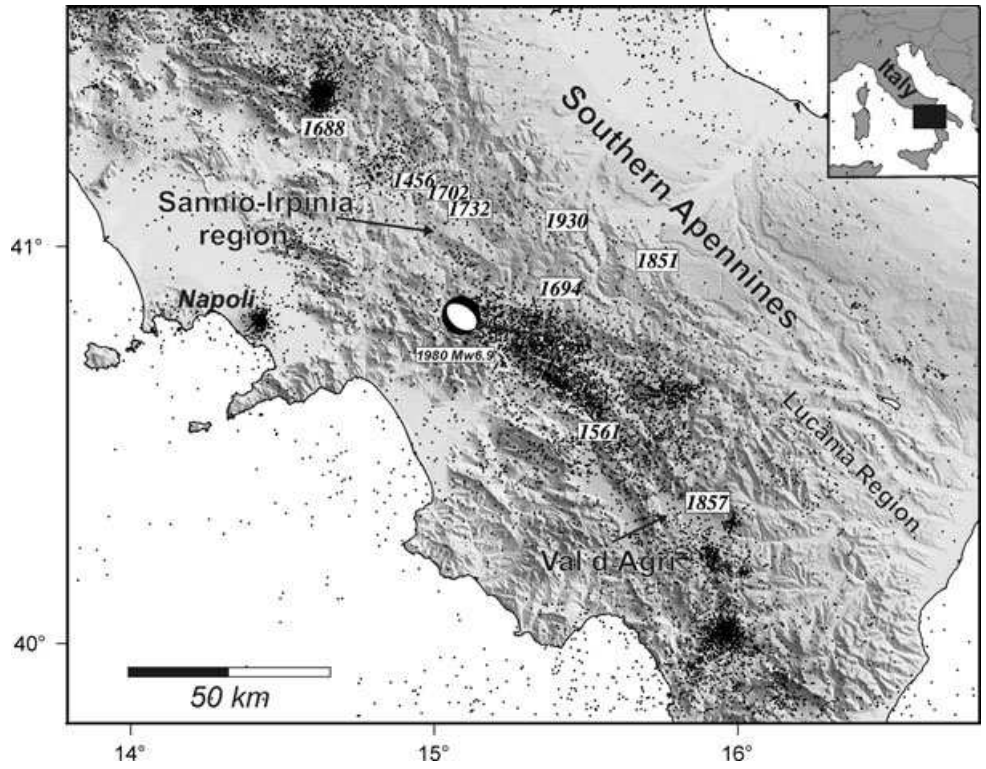

Figure 1. Map of the Southern Apennines seismic belt (see geographic location in the inset). Small black dots are the instrumental seismicity recorded by the Centralised National Seismic Network (RSNC) during the past 20 yr (Castello *et al.* 2006). White squares indicate historical seismic events with magnitude greater than 6.0 (from CFTI Boschi *et al.* 2000). The *M* 6.9 Irpinia earthquake focal mechanism solution is also reported (from the Harvard CMT Catalogue).

detected and pre-processed from the acquired data, to obtain earthquake locations and focal mechanisms and to investigate the space-time distribution of seismicity.

In several cases, small to moderate earthquakes have been associated with the poroelastic response of the crust to water level changes in reservoirs (Gupta *et al.* 1972; Gupta 1983, 1985; Simpson *et al.* 1988; Talwani 1997 and reference therein) or oil exploitation wells (Talebi *et al.* 1998; Zoback & Zinke 2002; Phillips *et al.* 2002; Ottemoller *et al.* 2005). The presence, in the Val d'Agri, of one of the most important on-shore European oil field (see productive wells in Fig. 2) and of a relatively large water reservoir (the Pertusillo Lake Dam, Fig. 2) can modify the seismic release and the occurrence of small to moderate earthquakes. Thus, we investigate the temporal and/or spatial relation between recorded seismicity and the human activities developed in the basin, to take into account the possible interpretation of the microseismicity as induced by the Pertusillo reservoir Dam and/or by exploitation of the Val d'Agri oil field.

2 SEISMOTECTONIC SETTING OF THE VAL D'AGRI BASIN

The Val d'Agri is a Quaternary intermountain basin, located in the axial zone of the Southern Apennines fold and thrust belt (Fig. 1). The upper crust is characterized by a complex pattern of thrusts, folds and normal faults reflecting the superposition of two main tectonic phases. Following Miocene–Early Pleistocene shortening responsible for the growth of the Southern Apennines thrust belt (Patacca *et al.* 1990; Menardi Noguera & Rea 2000; Catalano *et al.* 2004), the axial zone underwent NE–SW trending extension (Hippolyte *et al.* 1994). The bulk of Quaternary extension has been accommodated by major NW-trending transtensional and normal faults systems, which cross-cut the pre-existing contractional structures and, nowadays, bound large intermountain basins (Cinque *et al.* 1993). Focal mechanisms of moderate-large events (Gasparini *et al.* 1985; Westaway & Jackson 1987; Pondrelli *et al.* 2002), breakouts from deep wells (Amato & Montone 1997) and geodetic data (Hunstad *et al.* 2003; Ferranti *et al.* 2008) document that the NE–SW extension is still active, at a rate of 2–3 mm yr^{-1}.

Crustal seismicity recorded in the Southern Apennines during the last three decades concentrates within a 30–50 km wide and 15 km thick seismic belt along the axis range (Amato *et al.* 1997; Chiarabba *et al.* 2005; Fig. 1). Seismicity occurs either along the major seismogenic structures, such as the Irpinia Fault, which slipped during the 1980 Ms6.9 normal-faulting event, or at the boundary between adjacent fault segments of the active belt (Fig. 1). The continuity of the seismic belt is interrupted by two regions of scarce seismicity corresponding to the Sannio-Irpinia boundary and to the Val d'Agri area (Fig. 1).

Within and around the Val d'Agri basin, two main destructive events occurred in 1561 (Me 6.5) and in 1857 (*M*e 7.0; Boschi *et al.* 2000; Fig. 1). The macroseismic epicentre of the 1857 event, which struck the Val d'Agri, killing over 11 000 people (Branno *et al.* 1983), is localized just in the central part of the basin (Fig. 1). On the other hand, instrumental seismicity recorded in the Val d'Agri region in the past 20 yr is low and sparse (Chiarabba *et al.* 2005; Fig. 1). Only two small seismic swarms were recorded in 1996 April–June and 2002 February–December, during temporary regional passive surveys. The first swarm, accurately investigated by Cucci *et al.* (2004), was characterized by low-magnitude events (M_d = 1.8–3.4), to the south of the basin at 2–7 km depth. The

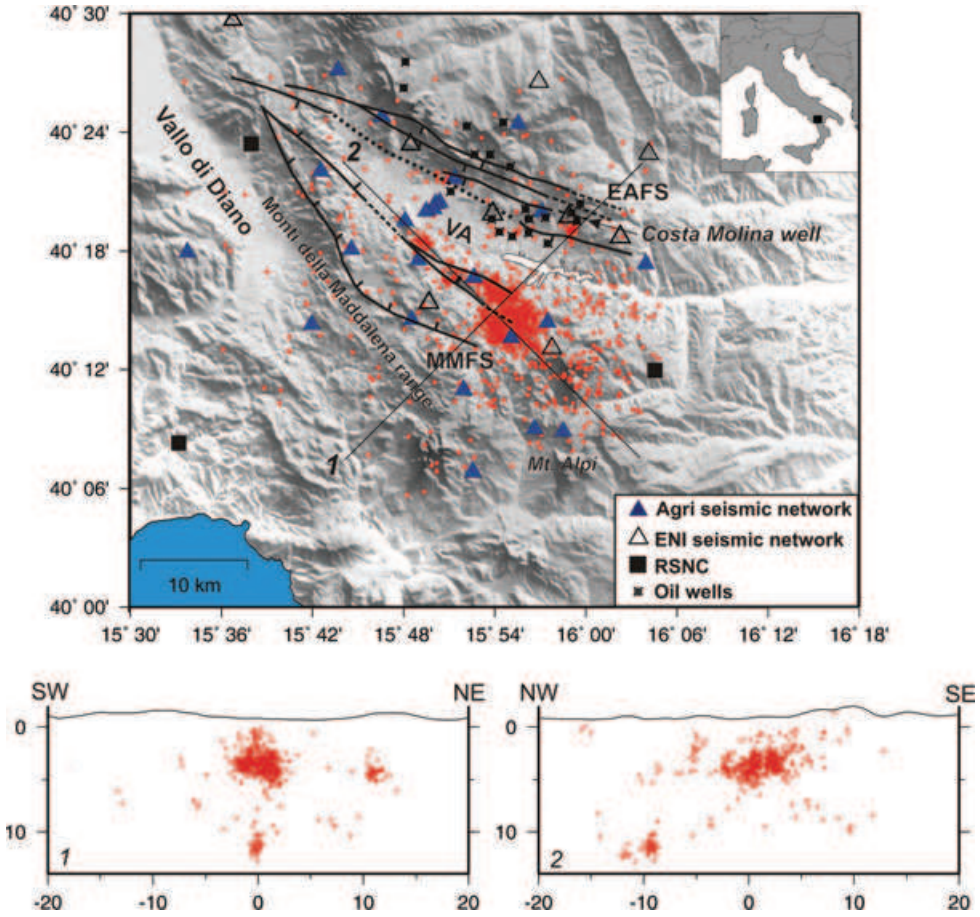

Figure 2. The Val d'Agri seismic network (blue solid triangles) along with stations of the Centralised National Seismic Network (RSNC; black solid squares) and of the Ente Nazionale Idrocarburi (ENI; black triangles) network. Red dots represent the location of 1994 earthquakes analysed in this study. Quaternary normal faults are from Maschio *et al.* (2005); EAFS, eastern Agri Fault System; MMFS, Monti della Maddalena Fault System. The location of the Pertusillo Lake is also reported. Black dots represent the location of productive wells of the Val d'Agri oil play redrawn from Holton (1999) and from the UNMIG Well Database available at http://unmig.sviluppoeconomico.gov.it/unmig/pozzi/pozzi.asp.

second swarm consists of very few earthquakes with magnitudes ranging between 2.2 and 3.2, clustering to the south of the Agri basin as well (Frepoli *et al.* 2005).

Seismogenic structures have been mainly proposed based on surface geologic and geomorphologic data (e.g. Cello *et al.* 2003; Maschio *et al.* 2005). The geometry and seismogenic potential of these structures are debated, and two opposing seismotectonic models have been proposed. Most authors (Benedetti *et al.* 1998; Cello & Mazzoli 1999; Borraccini *et al.* 2002; Cello *et al.* 2003; Barchi *et al.* 2006) consider a morphologically evident NW-trending and SW-dipping normal-fault system, bordering the basin to the east, as the main seismogenic structure (EAFS in Fig. 2).

Conversely, other investigators (Valensise & Pantosti 2001; Maschio *et al.* 2005; Burrato & Valensise 2008) ascribe the seismogenic potential of the area to a fault system located along the Monti della Maddalena ridge to the west of the basin (MMFS in Fig. 2). Maschio *et al.* (2005) proposed a poly-phase tectonic evolution of the basin. The EAFS played a primary role up to the Middle Pleistocene. According to Maschio *et al.* (2005), tectonic activity then shifted westwards within the Monti della Maddalena ridge, where the authors mapped a NW-trending and NE-dipping active normal-fault system (MMFS in Fig. 2) by means of morphostructural investigations.

3 THE SEISMIC SURVEY

Starting from 2005 May and for a period of 13 months, 23 continuously recording seismic stations were operating in the axial sector of the Lucania Apennines, within an area of about 1600 km^2 (blue solid triangles in Fig. 2). The investigated region includes, from east to west, the Val d'Agri basin, the Monti della Maddalena ridge, the southern sector of the Vallo di Diano basin, and extends southwards to the Monte Alpi massif (Fig. 2). The average receiver spacing is 5 km. The temporary network was complemented by six permanent stations of the RSNC (black solid squares in Fig. 2) and by the ENI local network (13 stations recording on trigger mode; black triangles in Fig. 2). The 23 stations were equipped with different digital acquisition systems (Reftek130 and Marslite88) and three-component short period sensors (Lennartz 3-D-1s and 5s). The stations recorded in continuous mode at a sampling rate of 125 Hz, to achieve a good sampling for local events. Solar panels were used to power the instruments and a GPS antenna provided the absolute timing and accurate location. Only 3 per cent of the data were lost during data retrieval process. We performed preliminary microtremors surveys to select optimal recording sites. All stations were installed on bedrock outcrops far from sources of anthropogenic noise, with the exception of four stations aimed at

investigating site effects in the central Val d'Agri basin (Fig. 2). Whenever possible, we included phase readings from waveforms by the permanent stations operating in the area (Fig. 2).

4 DATA ANALYSIS

4.1 Earthquake detection

The difficulty to manage a huge data set is commonly solved with automatic procedures that robustly scan the massive continuous records and detect microearthquakes (Bear & Kradolfer 1987; Scherbaum & Johnson 1992; Aster & Rowe 2000; Aldersons 2004; Di Stefano *et al.* 2006). To analyse the recorded data set, we developed an automatic procedure that smartly recognizes local earthquakes and furnishes consistently weighted *P*-wave arrival times (Aldersons 2004; Di Stefano *et al.* 2006). Phases identification was obtained via a Short time average/Long time average (Sta/Lta) ratio based algorithm at individual station. After performing numerous tests, the following values for trigger parameters were chosen: Sta/Lta ratio = 3; Sta = 2 s and Lta = 40s; duration = 2 s. The minimum number of triggers, used to declare a possible earthquake, was set to 4. The chosen parameters, together with the dense geometry of the seismic network, were effective to detect a huge number of very low magnitude earthquakes and discard false events (Fig. 3).

After events identification, we applied to the entire data set a recently developed picking system called 'MannekenPix' (hereinafter MPX; Aldersons 2004), described in Appendix A. This procedure allowed the picking and error assessment for ∼22 000 *P*-phase arrivals and preliminary locations for more than 2000 seismic events (Fig. 2). About 90 per cent of these events has a rms lower than 0.2 s (black histogram in Fig. 4a), hypocentres formal errors lower than 1 km, both in the vertical and horizontal direction (black histograms in Figs 4b and c), azimuthal gap lower than 260° (black histogram in Fig. 4f) and at least four *P*-wave readings.

From the entire data set, we selected 744 best-located events to hand-pick *S*-wave arrival times, according to the weighting scheme shown in Table 1. The selected data set, consisting of 10134 *P* and 9424 *S*-wave arrival times, is used to compute the 1-D velocity model and verify the automatic picking procedure.

4.2 1-D velocity model

We estimated the 1-D *P*-wave velocity model of the area by applying a non-linear inversion technique based on genetic algorithms (Sambridge & Gallagher 1993; Kim *et al.* 2006). The models are parameterized with 3 km thick layers. The best-fit model is searched by a global exploration of the models space, which does not require the use of *a priori* information (e.g. starting model). The inversion procedure is stopped when 70 per cent of the generated velocity models has an individual global misfit (e.g. global rms residuals) lower than 0.11 s (for more details about the inversion procedure and parameters setting, the reader can refer to Bagh *et al.* 2007, which applied this technique to microseismicity data collected in the central Apennines). Fig. 5(a) shows the best-fit 1-D model (thick black line) and the family of models having misfit values lower than 0.11 s (thin grey lines). The forward modelling is solved with the Hypoellipse code (Lahr 1989).

V_P values and layers thickness of the best-fit model are reported in Table 2. *P*-wave velocities increase from 4.3 km s^{-1} in the shallow layer to 6.8 km s^{-1} at 12 km depth. A low velocity layer (V_P = 5.9 km s^{-1}) is retrieved between 12 and 15 km depth. These V_P values are consistent with previous information on the velocity structure of the upper crust obtained by refraction surveys and velocity logs from deep wells in the Southern Apennines (Improta *et al.* 2002, 2003; Shiner *et al.* 2004). The V_P value of 4.3 km s^{-1} of the upper layer can be considered as a representative average between high-velocity (V_P = 5.0–6.0 km s^{-1}) basinal and shelf carbonates and low-velocity (V_P = 3.0–4.0 km s^{-1}) shales and siliciclastic deposits widely cropping out in the Lucania Apennines. From 3 to 9 km depth, the model shows *P*-wave velocities between 5.9 and 6.4 km s^{-1}. These values are consistent with the 6.0–6.2 km s^{-1} velocity range estimated for the Mesozoic limestones and dolomites of the Apulia Carbonate Platform, which forms the lower structural level of the thrust belt and has been drilled in the Val d'Agri area at 2–4 km below sea level (Menardi Noguera & Rea 2000; Dell'Aversana 2003). The V_P value of 6.8 km s^{-1} found between 9 and 12 km depth can be related to the deeper portion of the Apulia Platform, which consists of Triassic dolomites and anhydrites, with V_P values as large as 6.6–6.7 km s^{-1} (Bally *et al.* 1986; Improta *et al.* 2000). Finally, the velocity inversion at 12 km depth can be tentatively associated with low-velocity (V_P = 5.0–5.5 km s^{-1}) Permo-Triassic sediments imaged at the base of the Apulia Platform by commercial reflection profiles acquired in the Val d'Agri area (Shiner *et al.* 2004). However, we point out that V_P values within this low-velocity layer are poorly constrained, since only few events occurred at this depth range.

The mean V_P/V_S ratio for the study area has been computed by using the hand-picked *S* waves with the cumulative Wadati diagram (Fig. 5b). We estimated a V_P/V_S value of 1.90. This is in agreement with V_P/V_S values estimated in other seismic zones of the Apennines chain (e.g. Umbria-Marche seismic zone; Chiarabba & Amato 2003), but exceeds the value (1.82) reported by Frepoli *et al.* (2005) for a wider portion of the Lucania Apennines.

4.3 Earthquake locations

Using the improved velocity model and the hand-picked *S*-wave arrival times, we re-located the entire data set, and we discuss here the efficacy of the automatic procedure. After 1-D earthquake locations, almost all events have rms lower than 0.2 s (grey histogram in Fig. 4a), vertical and horizontal location errors lower than 0.3 km (grey histogram in Figs 4b and c) and azimuthal gaps smaller than 180° (grey histogram in Fig. 4f). *S*-wave residuals for the selected data set are also reported (Fig. 4e).

This approach allowed us to carry out an *a posteriori* test on the performance of the MPX procedure over a large subset of data. Results of this test show that MPX successfully recognized 7202 *P*-wave onsets, with respect to the 8131 waveforms of the Val d'Agri data set, corresponding to an efficiency of 88 per cent. Automatic picks and manual readings show a consistent distribution within the different weighting classes (see Table 3), a result that reveals the efficiency of the MPX calibration phase aimed at setting up the weighting engine of the automatic picking. Then, we computed the time differences between automatic pickings (AP) and manual pickings (MP) for the different weighting classes (Figs 6a–d). Although the difference between the AP and the MP for class 1 is in the ±0.05 s time range, about 92 per cent of picks fall in the ±0.025 s window (Fig. 6a), this latter corresponding to the class 1 error boundaries of the user defined weighting scheme (Table 1). Moving to the class 2, the time differences are within a ±0.1 s window, but about 90 per cent of data fall in the ±0.05 s range corresponding to the error boundaries set for class 2 (Fig. 6b). For class 3, we found the AP–MP difference in the window ±0,15 s with

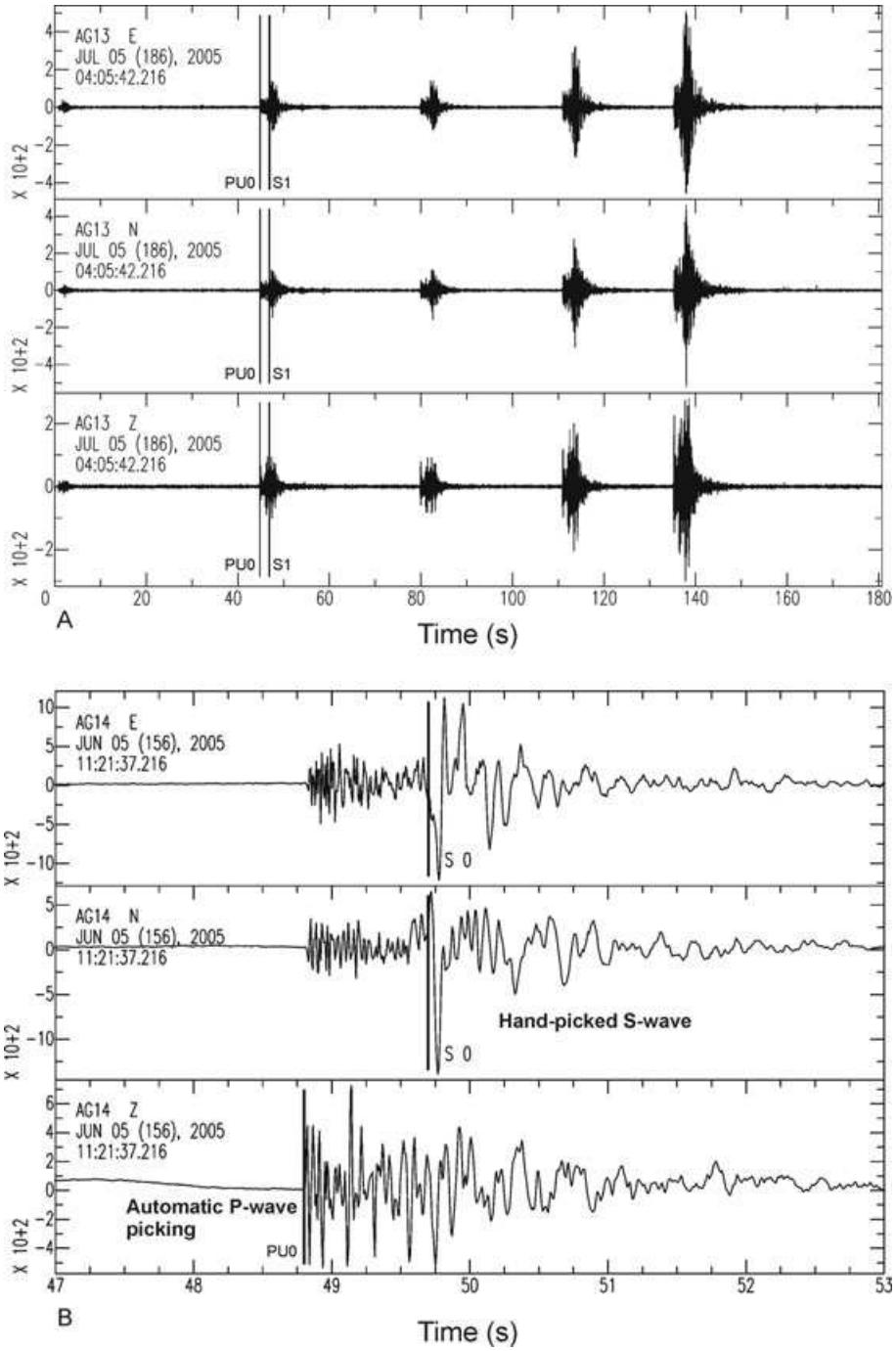

Figure 3. (a) Example of a waveform with multiple events. (b) Example of *P*- and *S*-wave readings.

about 95 per cent in the ± 0,1 s range (Fig. 6c). Finally, AP–MP for class 4 are lower than 0.4 s, with about 70 per cent in the window 0.1 s (Fig. 6d). These findings indicate that MPX yields reliable picks for classes 1, 2 and 3, whereas automatic picking accuracy is lower for class 4; this is probably due to the lower quality of the waveforms belonging to this weighting class. Finally, we compared the 1-D locations obtained using AP and MP arrival times for the 744 events (Fig. 6e). Both AP data (black histogram) and MP data (grey histogram) show a very similar hypocentre depth distribution (Fig. 6e). These results suggest the reliability of 1-D locations obtained by using MPX arrival times.

4.4 M_L Estimation

We calculated synthetic Wood–Anderson seismograms by removing the instrument response for each seismic record. Then, we convolved the displacement ground motion with the standard Wood–Anderson torsion seismograph response (Anderson & Wood 1925; Richter 1935). The maximum amplitude was measured after rotating each horizontal seismogram to the radial and transverse components. The computed magnitudes range between –0.19 and 2.74 and the completeness magnitude of the catalogue is equal to 0.4 (Fig. 7).

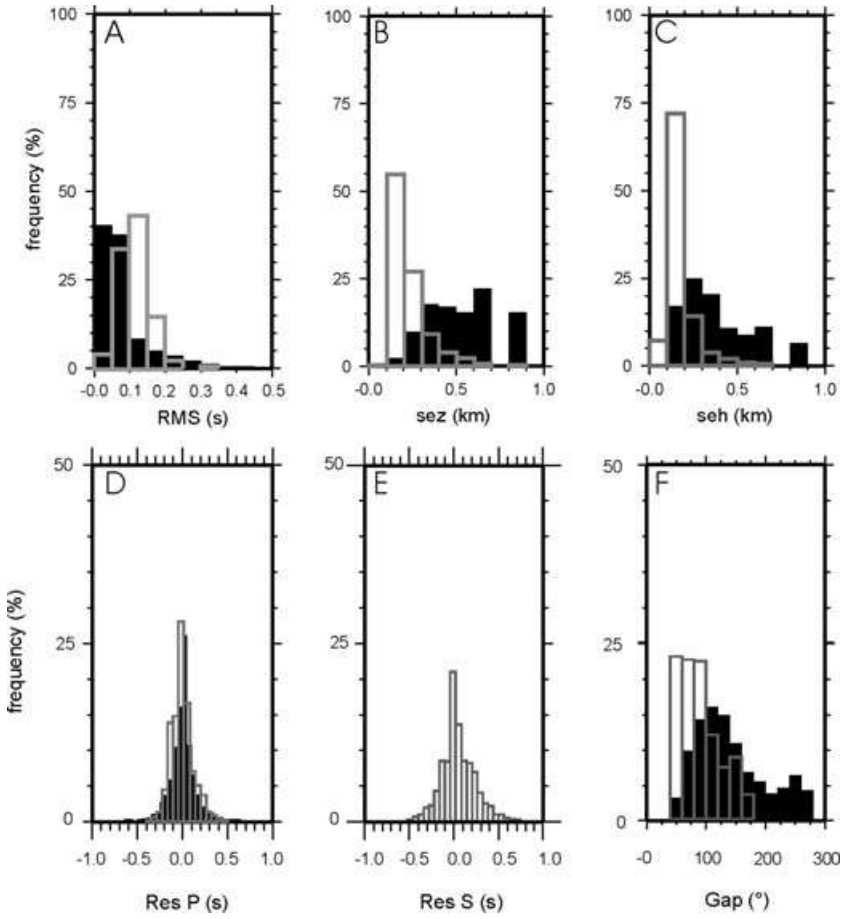

Figure 4. Histograms showing the location residuals (a) in seconds, horizontal (b) and vertical (c) errors (kilometres), *P*-residuals versus frequency (d) and azimuthal gaps (f) for events located using the MPX automatic pickings (black histograms) and for the 744 selected events (grey histograms) located using automatic *P*-wave pickings and manual *S*-waves pickings. Residuals for the hand-picked *S* waves for the selected 744 events are also shown (histogram e).

Table 1. Weighting scheme for the phase readings on the waveforms.

Class	Weight	Picking uncertainty (s)
1	0	0–0.025
2	1	0.025–0.05
3	2	0.05–0.1
4	3	>0.1

5 EARTHQUAKES DISTRIBUTION AND KINEMATICS

We investigate the earthquakes distribution with time by analysing the cumulative number of events (black line in Fig. 8) with respect to the number of events per day (grey line in Fig. 8). The average seismic release rate is 3.1×10^{-3} events d^{-1} km^{-2}, considering 1994 seismic events recorded in 396 d over a 1600 km^2 area (see Fig. 2). However, seismic release was not continuous during the experiment interval, as indicated by the significant variations in the rate curve in Fig. 8.

We distinguish four time intervals associated with distinct breaks in the curve slope (Fig. 8). From 2005 May till the end of 2005 July, we observe a moderate rate of seismic release with some peaks exceeding 10 earthquakes per day (phase 1). During the following five months, from 2005 August till the end of December, the seismic release was very low (i.e. the slope of the black curve decreases) (phase 2). Starting from 2006 January, the seismicity rate increases (phase 3), reaching the maximum between 2006 March and May (phase 4 is characterized by an evident increase of the seismicity rate starting from point C). This increase is due either to a general growth of the rate of seismic release or to the occurrence of small microseismic sequences (i.e. see the small sequences occurring during phases 3 and 4 in Fig. 8). A rapid decrease is observed from the second half of 2006 May and then an isolated peak occurs in 2006 June (see the last leg of the curve starting at point D in Fig. 8). An example of the intense rate of seismic release is shown in Fig. 3(a), where five small events ($-0.1 < M_L < 1.4$) occur in a 180 s long record section. They nucleate very close to each other, showing a swarm-like activity.

Fig. 2 shows the spatial distribution of the 1994 recorded seismic events. Most of the earthquakes are located beneath the southwestern side of the basin between 2 and 6 km depth, whereas few events occur along the north-eastern side (cross-sections 1 and 2 in Fig. 2). Very few earthquakes occur in the 10–12 km depth range (cross-section 1 in Fig. 2).

The correlation between the recorded seismicity and the Quaternary normal faults is emphasized by the spatial distribution of the 744 selected events (Fig. 9). A ∼5 km wide cluster of intense microseismicity is located at the southern termination of the MMFS, to the south of the basin, between 2 and 6 km depth. Earthquakes are widespread in this volume, without enlightening any clear fault plane (see the NE-striking cross-section 9 in Fig. 9). The seismic

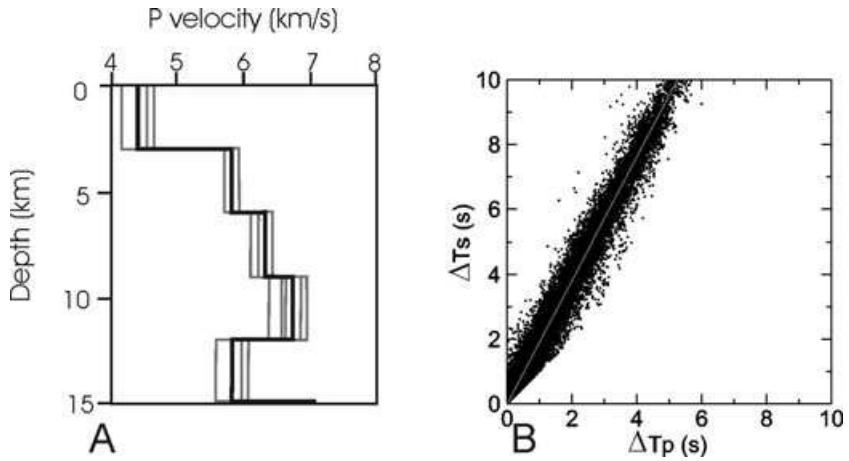

Figure 5. (a) *P*-wave best velocity model (thick black line) and models with misfit values lower than 0.1077 s (thin grey lines); (b) Wadati diagram. The computed V_P/V_S ratio is equal to 1.90.

Table 2. 1-D *P*-wave velocity model and ranges of search width for velocity values in the different layers.

Layer	Velocity range	Depth to the layer top (km)	Velocity (km s^{-1})
1	3.5–5.5	0–3	4.33
2	4.0–6.5	3–6	5.92
3	4.0–6.5	6–9	6.42
4	5.0–7.0	9–12	6.85
5	5.0–7.0	12–15	5.93
6	6.5–7.5	> 15	7.00

Table 3. Performance table showing the distribution of the MPX (AP) and manual (MP) readings among the different weighting classes.

	Manual pickings	MPX pickings
Number of waveforms	8131	7202
Class 1	2989 (36.76 per cent)	2451 (34.04 per cent)
Class 2	2604 (32.02 per cent)	2733 (37.94 per cent)
Class 3	1750 (21.52 per cent)	1407 (19.53 per cent)
Class 4	787 (9.67 per cent)	611 (8.48 per cent)

release is very high, showing a prevalent swarm-type activity with low-magnitude earthquakes ($M_L \leq 2.1$) released through the occurrence of small sequences not associated with an identifiable main shock (see the small sequences occurring during phases 3 and 4 in Fig. 8).

Along the western margin of the basin, hypocentral alignments reveal the presence of a planar surface that dips ∼50° northeastwards down to 6 km depth (cross-section 7 in Fig. 9). A second small cluster of microearthquakes (M_L between 1.02 and 2.11) is located between 10 and 12 km depth. These events are preferentially aligned along a vertical plane (cross-sections 1, 3 and 4 in Fig. 9).

Along the northeastern border of the basin, the seismicity is scarce. Only a small cluster of $M_L < 1.75$ events has been recorded at the southern termination of the EAFS between 3 and 5 km depth (cross-sections 5 and 6 in Fig. 9).

Earthquakes distribution versus depth (histogram in Fig. 9) delineates an about 12 km thick seismogenic layer, also recognizable in the two main cross-sections comprising all the recorded seismicity (cross-sections 1 and 2 in Fig. 9). The histogram shows a bimodal distribution: while about 90 per cent of the recorded seismicity is confined within the shallow crust between 2 and 6 km depth, the main contribution to the deeper peak derives from the cluster located along the western side of the basin with hypocentres in the 10–12 km depth range (cross-sections 3 and 4 in Fig. 9). This finding underlines the presence of a zone, between 7 and 10 km depth, where the seismic release is almost absent.

We computed focal mechanisms for 110 best-located events by using the *P*-wave first motion polarity method (FPFIT code; Reasenberg & Oppenheimer 1985). We choose focal mechanism solutions with less than two discrepancies and with a minimum number of *P*-wave polarities equal to 15. In Fig. 10, we show 51 focal mechanisms out of the computed 110, for the largest magnitude events. These focal mechanisms can be considered representative of the 110 solutions of the whole data set. About 70 per cent shows a dominant normal solution (black focal mechanisms in Fig. 10). In particular, 45 per cent is normal (rake between –60° and –120°) with about 7 per cent of pure normal events (see histogram c in Fig. 10). About 23 per cent is oblique/normal (grey focal mechanisms in Fig. 10).

A prevalent normal kinematics characterizes seismic events located along the western margin of the basin (Fig. 10 and cross-section in Fig. 11). These events show fault plane solutions striking about N130°E, dipping in the 50°–60° range, with a normal component kinematics (see black focal mechanisms in Fig. 10). Focal mechanisms for the events located in the main cluster to the south of the basin show both normal and strike-slip kinematics and variable values of strike and dip, suggesting that the deformation is accommodated in a volume rather than on a single planar structure (Fig. 10). Earthquakes related to the deep cluster of events (cross-sections 1, 3 and 4 in Fig. 9) show a pure normal kinematics with focal planes striking roughly N20°E (map in Fig. 10). The small cluster of events, located between 3 and 5 km depth along the eastern side of the basin, has a prevalent strike-slip kinematics (Fig. 10).

6 SEISMICITY NEAR THE PERTUSILLO RESERVOIR

The cluster located to the south of the Val d'Agri basin is characterized by the occurrence of a large number of shallow (2–6 km) low magnitude ($M_L \leq 2.1$) events. This cluster extends from 3 to 9 km to the south of the Pertusillo reservoir (see Figs 2 and 12). Low magnitude earthquakes occurring at shallow depths mimicking a swarm-type activity are commonly observed in reservoir-induced seismicity examples (Gupta *et al.* 1972; Gupta 1983, 1985; Simpson *et al.* 1988; Piccinelli *et al.* 1995; Talwani 1997 and

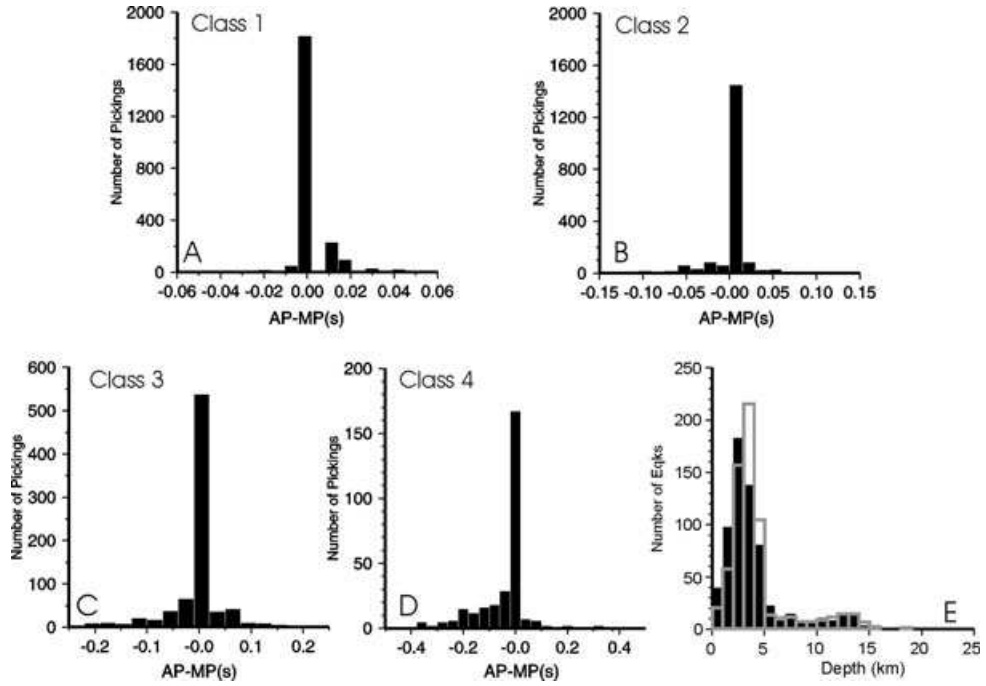

Figure 6. Distribution of time differences (in seconds) between MPX arrival times (AP) and manual picks (MP) within each weighting classes (histograms a–d); the histogram (e) shows the distribution with depth obtained using AP (black histogram) and MP (grey line histogram) arrival times for the 744 events.

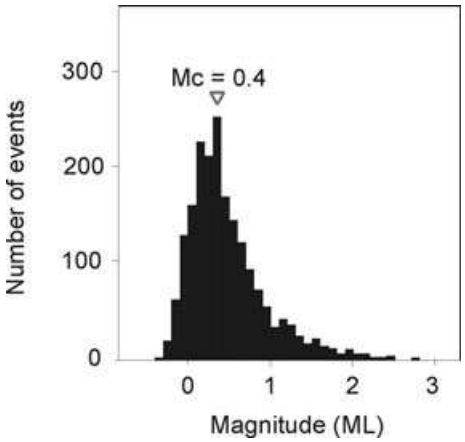

Figure 7. The histogram shows the number of events for different classes of magnitude. The completeness magnitude (M_C) is also reported.

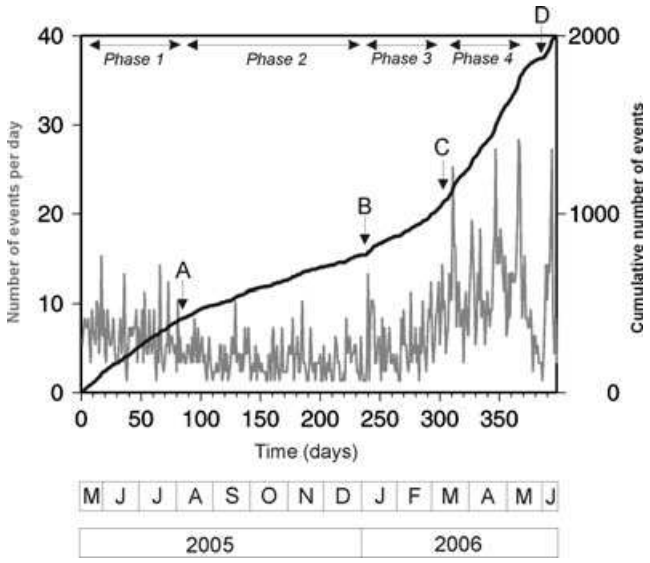

Figure 8. Cumulative number of seismic events versus time (black line) and number of events per day (grey line). Four different time intervals characterized by a different rate of seismic release are shown (see text for further details). Arrows outline main changes in the slope of the black line.

reference therein). In this section, we investigate the correlation between the water level changes in the Pertusillo reservoir and the seismic activity of this cluster (Fig. 12).

The Pertusillo Lake Dam, completed in 1963, is 95 m high and can store up to 155 million m^3 of water. The reservoir covers an area of about 75 km^2 (Fig. 12) and is characterized by large and rapid seasonal water level oscillations as high as 40 m, which correspond to a variation in the reservoir storage of about 80 million m^3 (i.e. about half of the reservoir storage).

In Fig. 12 we compare the water level change of the reservoir from 2004 April to 2006 June (i.e. a time window that includes the seismic experiment and the year before; Fig. 12a) with the seismicity rate for this cluster (Fig. 12b). The lake level shows an evident annual cycle change: the lake level rapidly rises from November to March, and slowly lowers from June to October-November. During the reservoir re-filling in fall-winter 2005, the water level increase is very rapid and large (14 m).

The comparison shows that seismicity seems to be positively correlated with water level oscillations. An increased rate of seismicity accompanies the lake level rise and vice versa (Figs 12 a and b). Besides, the maximum seismicity rate is reached between 2006 April to May, when the reservoir re-filling is complete and the water level is stable.

The comparison with the curve showing the cumulative number of events with time is enlightening (Fig. 12b). We note four breaks in

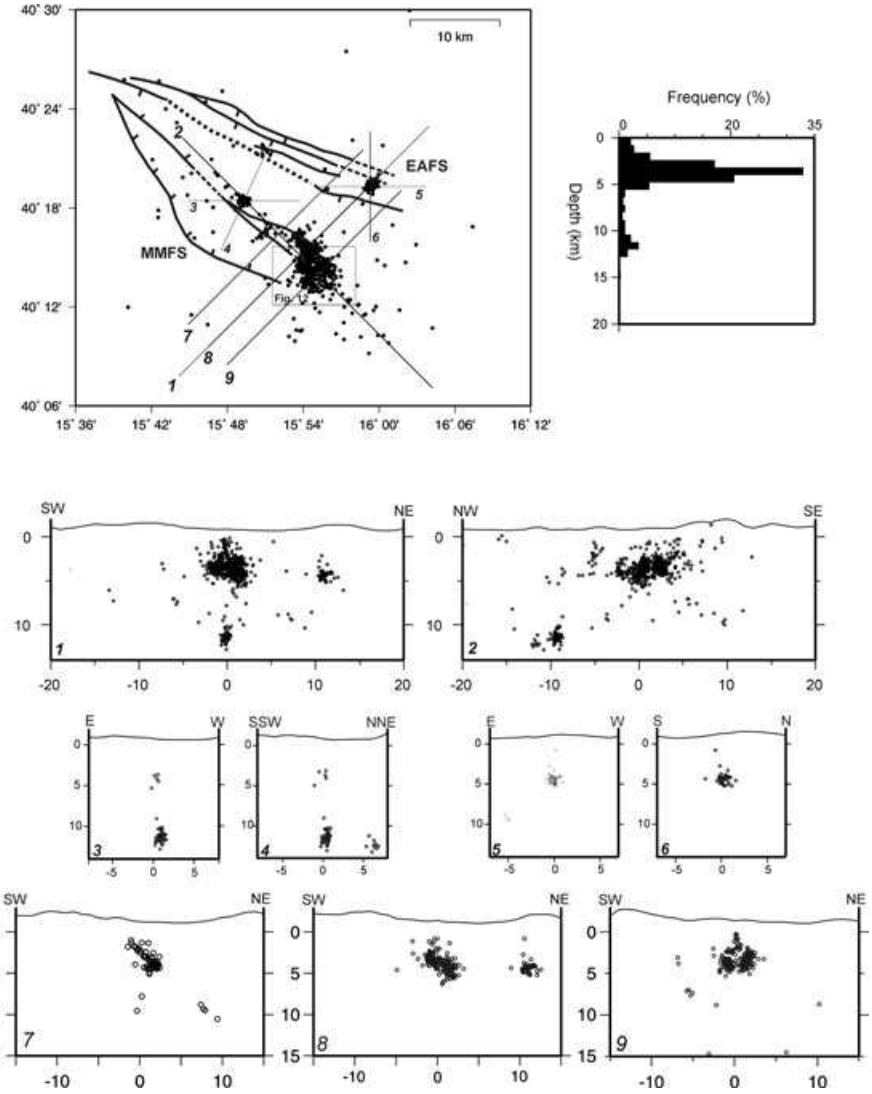

Figure 9. Map and cross-section view of the selected 744 seismic events. The NW–SE and NE–SW striking vertical cross-sections (1 and 2) comprise all the earthquakes shown in map. The small cross-sections (3–6) show hypocentral locations for events related to the two small clusters of events located along the western (sections 3 and 4) and eastern (sections 5 and 6) side of the basin. Cross-sections (7–9) show hypocentral locations for the events located along the south-western side of the basin. The seismicity map also reports the main Quaternary fault systems from Maschio *et al.* (2005). EAFS, eastern Agri Fault System and MMFS, Monti della Maddalena Fault System. (b) histogram showing the distribution with depth of the recorded seismicity.

the slope of the cumulative seismicity curve, separating four phases of different seismic release. During the first phase, a quite high seismic release accompanies the high lake level. The subsequent reservoir unloading (A′–B′ curve in Fig. 12a) corresponds to strong decrease of the seismic release (phase 2, from A to B in Fig. 12b), with an almost instantaneous response (the elapsed time between the points A′ and A is about 10 d). Starting from the end of 2005 November, the very rapid and pronounced increase in the water level (point B′ in Fig. 12a) is followed by a second break in the seismicity curve (point B in Fig. 12b); the slope of the seismicity curve gently increases as well as the seismic release (phase 3 in Fig. 12b). We observe a quasi-instantaneous response of the system to the rise of water level in the reservoir, since the elapsed time between B′ and B is about 10 d. The instantaneous response is even clearer when a second rapid increase in the water level curve occurs (point C′ in Fig. 12a): the seismicity curve shows a rapid increase with a strong break in the slope of the cumulative curve (point C in Fig. 12b). Then, the reservoir experiences an almost stable and high water level until the point D′ (Fig. 12a). During phase 4 (from C to D in Fig. 12b), the seismic release is very high and characterized by microsequences; this phase lasts up to 100 d after point C′. The seasonal unloading phase starts around the third week of 2006 May (point D′ in Fig. 12a) and is accompanied by quasi-instantaneous and strong decrease in seismic release (point D in Fig. 12b).

Thus, the positive correlation found between seismicity rate and loading/unloading phases in the nearby reservoir leads us to interpret the cluster as reservoir induced seismicity.

7 DISCUSSION

7.1 Seismicity and active faults

The thickness of the seismogenic layer bounded by the seismicity cut-off is about 12 km (see histogram in Fig. 9). This value is in agreement with previous estimates for the Southern Apennines

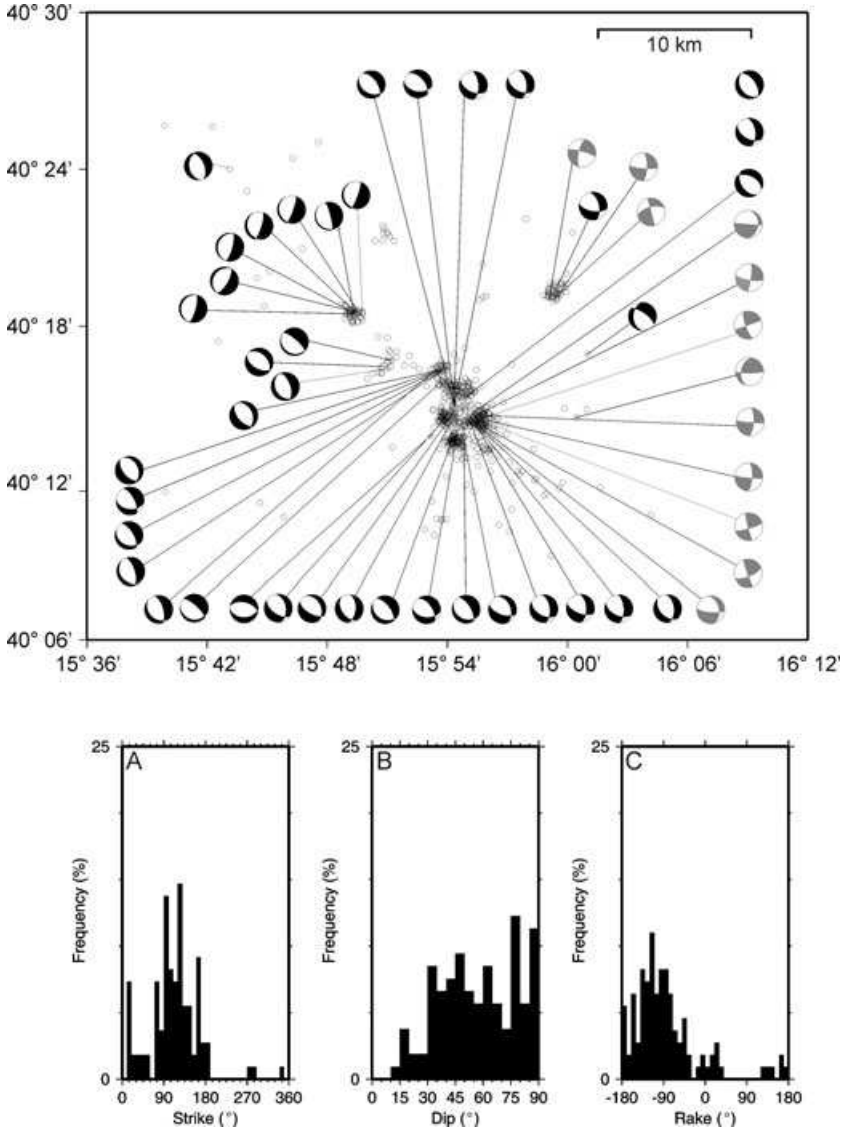

Figure 10. Map showing focal mechanisms for 51 selected seismic events; grey focal solutions represent oblique and strike-slip kinematics. Histograms show strike (a), dip (b) and rake (c) values for the 110 computed focal mechanisms.

seismic belt (Chiarabba & Amato 1994; Amato *et al.* 1997; Chiarabba *et al.* 2005) and is consistent with the fault width dimension of the two largest instrumental earthquakes of the Southern Apennines (i.e. the 1980 M_s 6.9 Irpinia earthquake, Westaway & Jackson 1987; and the 1930 M_w 6.5 Irpinia earthquake, Pino *et al.* 2008). However, most of the seismicity is shallow, and we suppose that it occurs within the limestone of the Apulia Carbonate Platform, whose top has been drilled in this area between 2 and 4 km below sea level (Menardi Noguera & Rea 2000; Dell'Aversana 2003).

Events concentrate beneath the southwestern margin of the Val d'Agri basin, mostly within a NW-striking, about 10 km long and 5 km wide volume (Fig. 9). Focal mechanism solutions show a prevalent normal kinematics (Fig. 10) consistent with the extensional stress field (NE-trending $\sigma 3$) estimated by borehole breakouts, regional focal mechanisms (Cucci *et al.* 2004) and field studies (Maschio *et al.* 2005). To the NW of this volume, microseismicity reveals a 50°NE-dipping plane, between 1 and 6 km depth, with a clear normal-faulting kinematics (Fig. 11). The upward continuation of this fault plane coincides with the trace of the Monte Aquila Fault (thick black line in Fig. 11), the main southern strand of the MMFS (Maschio *et al.* 2005). Our result supports the contention that this fault is active, extending and corroborating field data and shallow seismic prospecting, indicating coseismic faulting in Late-Pleistocene Holocene deposits (Maschio *et al.* 2005; D'Addezio *et al.* 2006; Improta & Bruno 2007).

The reservoir induced swarm-like seismicity concentrates at the southern termination of the MMFS. Here, the seismic deformation, showing a great variability in strike, dip and rake of focal planes, is not confined on a single plane but is accommodated on very small and shallow segments in the hanging wall of the MMFS.

Few events occur at 10–12 km depth, beneath the central sector of the basin (cross-sections 1, 3 and 4 in Fig. 9). Hypocentres are mainly elongated on a vertical plane, and focal mechanisms show an almost dip-slip kinematics on planes striking N20°E. We tentatively interpret this structure as a pre-existing compressive or strike-slip structure in the deep Apulian units (Shiner *et al.* 2004), reactivated with dip-slip kinematics in the present SW–NE extensional field.

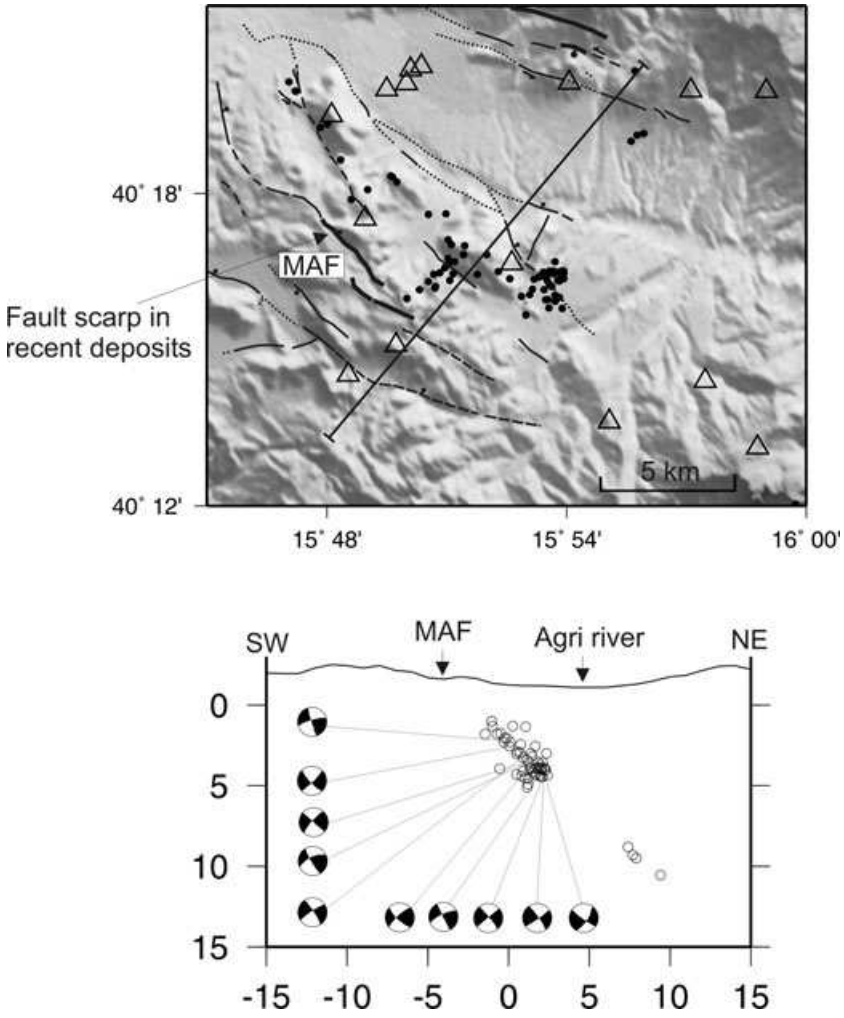

Figure 11. Map and cross-section view of the Monte Aquila Fault seismicity. The cross-section also reports some focal mechanism solutions.

Seismicity is almost absent at the NE border of the basin, with the exception of about 50 events located to the south of the EAFS (cross-sections 5 and 6 in Fig. 9), with focal mechanisms showing a prevailing strike-slip kinematics (Fig. 10). This cluster can be reasonably ascribed to the oil exploitation in the Val d'Agri fields, which extend between the NE margin of the basin and the nearby ridge (Fig. 2; see Holton (1999) for more details on the Val d'Agri oil play). In fact, event locations match very well, the easternmost productive wells (Costa Molina 2 well in Fig. 2). Furthermore, events concentrate in the 3–5 km depth range, consistent with the depth of the productive Apulian reservoir drilled by this well at ∼4 km depth (UNMIG Well Database; available at http://unmig.sviluppoeconomico.gov.it/unmig/pozzi/pozzi.asp).

The majority of microseismicity occurs on the MMFS, but this observation cannot discriminate which is the major fault responsible for the deformation of the Val d'Agri basin between the two SW- or NE-dipping alternative models, that is, EAFS (Benedetti *et al.* 1998; Cello *et al.* 2003) and MMFS (Maschio *et al.* 2005; Burrato & Valensise 2008). The EAFS may be presently locked, without microearthquake release. On the other hand, the MMFS may be partially locked, as suggested by the absence of seismic events at depths (i.e. 6–10 km), where the large normal-faulting earthquakes in the Southern Apennines usually nucleate (i.e. Cocco & Pacor 1993; Chiarabba & Amato 1994).

7.2 Reservoir induced seismicity

Reservoir induced seismicity can be classified into two categories: initial seismicity and protracted seismicity (Talwani 1997). The initial seismicity is the most commonly observed, and it is associated with the initial impoundment and/or with great and rapid water level changes in the reservoir. It results from an instantaneous effect of loading (or unloading) and a delayed effect due to pore pressure diffusion (Gupta *et al.* 1972; Simpson *et al.* 1988; Talwani 1997). The protracted seismicity is rarely observed because it is related to both the amplitude and frequency of the reservoir oscillation and the poroelastic properties of the subsurface rocks (e.g. the Lake Mead, U.S.A. and Koyna Reservoir, India; Gupta 1985).

In the Pertusillo reservoir, the seasonal water level variation reaches 40 m, with a maximum water height of 95 m. Such variation is in the range of those usually observed to induce seismic activity worldwide (Gupta 1985; Talwani 1997). The instantaneous seismicity response to the reservoir water level change and the occurrence of widespread low-magnitude earthquakes to the periphery of the reservoir suggest that the induced seismicity is classifiable as initial seismicity, driven by the rapid and large water level changes (see Talwani 1997). We hypothesize that the instantaneous effect of the system to rapid water level changes is interpretable as an 'undrained response' to the very rapid loading phase (see the seismicity curve

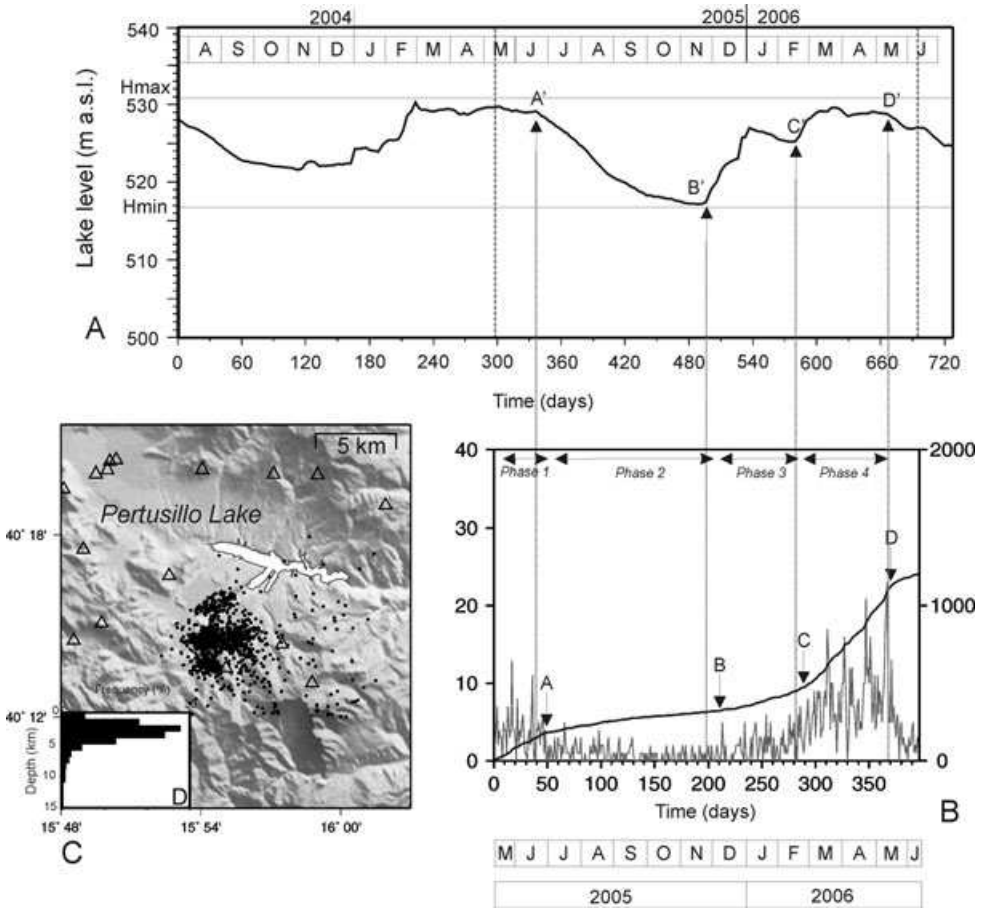

Figure 12. The figure investigates the relation between the water level (a) in the Pertusillo Lake Dam during the 2004 to 2006 period and the seismicity curve (b) for the selected cluster of events; (c) map view of the selected events; (d) frequency distribution at depth.

breaks at the B and C points; Fig. 12b). On the other hand, the sustained seismic release (curve C–D in Fig. 12b), characterized by the occurrence of microsequences up to 100 d after the increase in the water level (e.g. after the point C′ in Fig. 12a in), is imputable to a delayed effect, likely related to the pore pressure diffusion in the volume (see Talwani 1997). The same is valid for the unloading curve, even if this process appears to occur more slowly (e.g. see the curve A′–B′ Fig. 12a).

The reservoir induced seismicity location is generally governed by the nature of faulting below or at the edge of the reservoir (Gupta 1985; Simpson *et al.* 1988; Talwani 1997). In particular, Roeloffs (1988), investigating the role of an oscillating reservoir relative to the nearby faults, found that a reservoir located in the hanging wall of a normal fault has a destabilization effect on the normal fault system, striking parallel to the lake. This is perfectly compatible with locations (Fig. 12) and focal mechanisms (Fig. 10) observed to the south of the basin.

8 CONCLUSIONS

The seismicity is distributed in a NW-trending volume along the western flank of the Val d'Agri basin. To the south, intense swarm-type microseismicity defines a major cluster, ∼5 km wide, from 1 to 5 km depth, whereas in the central portion, earthquakes with a clear normal-faulting kinematics are aligned along a 50°NE-dipping plane between 1 and 6 km depth, defining an active normal fault. The upward continuation of this structure coincides with an active strand of the Monti della Maddalena (or western) normal fault system. On the contrary, the eastern fault system appears to be aseismic during the 1-yr-long experiment.

Nevertheless, this observation is not sufficient to define which fault system is accumulating significant deformation and establish the hierarchy between the two faults bounding the basin. As a consequence, we cannot propose a unique seismogenic source for the *M* 7.0 1857 event, which remains undefined.

We find a positive correlation between the rapid water level changes in the nearby Pertusillo reservoir and the intense swarm-type seismicity rate of the cluster located to the south of the basin. We interpret this seismic activity as a clear example of reservoir induced seismicity. The loading/unloading phases of the reservoir generate subsequent poroelastic effects, which seem to mould the seismic rate changes. We still do not know the physical processes that govern the initiation, propagation and arrest of the seismic rupture on a fault plane. For this reason, we cannot exclude that, in the future, these induced minor ruptures may dynamically trigger a larger event on the closest (i.e. western) fault system, which is also favourable oriented with the local stress field.

ACKNOWLEDGMENTS

We thank the Associate Editor and two anonymous reviewers for the thoughtful comments and suggestions that helped us to improve the

manuscript. We also thank the technical staff at the National Institute of Geophysics and Volcanology and all those who participated to the field work. We also thank P. De Gori and M. Moretti for their useful comments and suggestions and F. Aldersons for the MannekenPix procedure. L.V. was founded by the Università degli Studi di Napoli Federico II, during her PhD thesis, and by an INGV fellowship funded by the MIUR-FIRB project Airplane (RBPR05B2ZJ).

REFERENCES

Aldersons, F., 2004. Toward a three-dimensional crustal structure of the Dead Sea region from local earthquake tomography, *PhD thesis*. Tel Aviv University.

Allen, R., 1978. Automatic earthquake recognition and timing from single traces, *Bull. seism. Soc. Am.,* **68,** 1521–1532.

Allen, R., 1982. Automatic phase pickers: their present use and future prospects, *Bull. seism. Soc. Am.,* **72,** 225–242.

Amato, A. & Montone, P., 1997. Present day stress field and active tectonics in southern peninsular Italy, *Geophys. J. Int.,* **130,** 519–534.

Amato, A., Chiarabba C. & Selvaggi G., 1997. Crustal and deep seismicity in Italy (30 years after), *Ann. Geofis.,* **40–5,** 981–994.

Anderson, J.A. & Wood, H.O., 1925. Description and theory of the torsion seismometer, *Bull. seism. Soc. Am.,* **15,** 1–72.

Aster, R. & Rowe, C., 2000. Automatic phase pick refinement and similar event association in large seismic datasets, in *Advances in Seismic Event Location, Modern approaches in geophysics,* Vol. 18, pp. 231–263, eds Thurber, C.H. Rabinowitz, N., Kluwer Academic Publishers, Dordrecht, The Netherlands.

Bagh, S., Chiaraluce L., De Gori P., Moretti M., Govoni A., Chiarabba C., Di Bartolomeo P. & Romanelli M., 2007. Background seismicity in the Central Apennines of Italy: the Abruzzo region case study, *Tectonophysics,* **444,** 80–92.

Bally, A.W., Burby, L., Cooper, C. & Ghelardoni, R., 1986. Balanced sections and seismic reflection profiles across the Central Apennines, *Boll. Soc. Geol. It.,* **35,** 237–310.

Barchi, M., Amato, A., Cippitelli, G., Merlini, S., & Montone, P., 2006. Extensional tectonics and seismicity in the axial zone of the Southern Apennines, in *CROP-04,* Vol. 7, pp. 47–56, eds Mazzotti, A., Patacca, E. & Scandone, P., Boll. Soc. Geol. It., Spec. Issue.

Bear, M. & Kradolfer, U., 1987. An automatic phase picker for local and teleseismic events, *Bull. seism. Soc. Am.,* **77,** 1437–1445.

Benedetti, L., Tapponier, P., King, G.C.P, & Piccardi, L., 1998. Surface rupture due to the 1857 Southern Italian Earthquake, *Terra Nova,* **10**(4), 206–210.

Borraccini, F., De Donatis, M., Di Bucci, D., & Mazzoli, S., 2002. 3D Model of the active extensional fault system of the high Agri River valley, Southern Appennines, Italy, *J. Virtual Expl.,* **6,** 1–6.

Boschi, E., Guidoboni, E., Ferrari, G., Mariotti, D., Valensise, G. & Gasperini, P., 2000. Catalogue of strong Italian earthquakes from 461 B.C. to 1997 (version III), *Ann. Geophys.,* **43,** 1–259 (available on CD-ROM).

Branno, A., Esposito, E.G.I., Marturano, A., Porfido, S., & Rinaldis, V., 1983. Studio, su base macrosismica, del terremoto della Basilicata del 16 Dicembre 1857, *Boll. Soc. Natur. di Napoli.,* **92,** 249–338.

Butler, R.W. H. *et al.*, 2004. Applying thick-skinned tectonic models to the Apennine thrust belt of Italy—limitations and implications, in *Thrust Tectonics and hydrocarbon Systems,* Vol. 82, pp. 647–667, ed. McClay, K.R., AAPG Memoir.

Burrato, P., & Valensise, G., 2008. Rise and fall of a hypothesized seismic gap: source complexity in the *M*w 7.0 16 December 1857 Southern Italy Earthquake, *Bull. seism. Soc. Am.,* **98,** 139–148, doi:10.1785/0120070094.

Castello, B., Selvaggi, G., Chiarabba, C. e Amato, A., 2006. *CSI Catalogo della sismicità italiana 1981–2002,* version 1.1, INGV-CNT, Roma, available at http://www.ingv.it/CSI/.

Catalano, S., Monaco, C., Tortorici, L., Paltrinieri, W. & Steel, N., 2004. Neogene-Quaternary evolution of the Southern Apennines. *Tectonics,* **23,** TC2003, doi:10.1029/2003TC001512.

Cello, G. & Mazzoli, S., 1999. Apennine tectonics in southern Italy: a review. *J. Geodyn.,* **27,** 191–211.

Cello, G., Tondi E., Micarelli L. & Mattioni L., 2003. Active tectonics and earthquake sources in the epicentral area of the 1857 Basilicata earthquake (Southern Italy), *J. Geodyn.,* **36,** 37–50.

Chiarabba, C. & Amato, A., 1994. From tomographic images to fault heterogeneities, *Ann. Geophys.,* **37–6,** 1481–1494.

Chiarabba, C. & Amato, A., 2003. Vp and Vp/Vs images in the Mw 6.0 Colfiorito fault region (central Italy): a contribution to the understanding of seismotectonic and seismogenic processes, *J. geophys. Res.,* **108,** doi:10.1029/2001JB001665.

Chiarabba, C., Jovane, L. & Di Stefano, R., 2005. A new view of Italian seismicity using 20 years of instrumental recordings, *Tectonophysics,* **395,** 251–268.

Chiaraluce, L., Chiarabba, C., Collettini, C., Piccinini, D. & Cocco, M., 2007. Architecture and mechanics of an active low-angle normal fault: Alto Tiberina Fault, northern Apennines, Italy, *J. geophys. Res.,* **112,** B10310, doi:10.1029/2007JB005015.

Cinque, A., Patacca, E., Scandone, P. & Tozzi, M., 1993. Quaternary kinematic evolution of the Southern Apennines: relationships between surface geological features and deep lithospheric structures, *Ann. Geofis.,* **36,** 249–259.

Cocco, M. & Pacor, F., 1993. The rupture process of the 1980 Irpinia, Italy, earthquake from the inversion of strong motion waveforms, *Tectonophysics,* **218,** 1–3, 157–177.

Cucci, L., Pondrelli, S., Frepoli, A., Mariucci, M.T. & Moro, M., 2004. Local pattern of stress field and seismogenic sources in Melandro Pergola basin and in Agri valley (Southern Italy), *Geophys. J. Int.,* **156,** 575–583.

D'Addezio, G., Karner, B.D., Burrato, P., Insinga, D., Maschio, L., Ferranti, L. & Renne, P.R., 2006. Tephrochronology in faulted Middle-Pleistocene tephra layer in the Val d'Agri area (southern Italy), *Ann. Geophys.,* **40,** 1029–1040.

Dell'Aversana, P., 2003. Integration loop of 'global offset' seismic, continuous profiling magnetotelluric and gravity data, *First break,* **21,** 32–41.

Di Stefano, R., Aldersons, F., Kissling, E., Baccheschi, P., Chiarabba, C. & Giardini, D., 2006. Automatic seismic phase picking and consistent observation error assessment; application to the italian seismicity, *Geophys. J. Int.,* **165–1,** 121–134.

Eberhart-Phillips, D. & Michael, A.J., 1993. Three-dimensional velocity structure, seismicity and fault structure in the Parkfield region, central California, *J. geophys. Res.,* **98,** 15 737–15 758.

Ferranti, L. *et al*., 2008. Active deformation in Southern Italy, Sicily and southern Sardinia from GPS velocities of the Peri-Tyrrhenian Geodetic Array (PTGA), *Boll. Soc. Geol. It. (Ital.J.Geosci.),* **172**(2), 299–316.

Frepoli, A., Cinti, F.R., Amicucci, L., Cimini, G.B., De Gori, P. & Pierdominici, S., 2005. Pattern of seismicity in the lucanian Apennines (Southern Italy) from recording by SAPTEX temporary array, *Ann. Geophys.,* **48,** 1035–1054.

Gasparini, C., Iannaccone, G. & Scarpa, R., 1985. Fault-plane solutions and seismicity of the Italian peninsula, *Tectonophysics,* **117,** 59–78.

Gupta, H.K., 1983. Induced seismicity hazard mitigation through water level manipulation at Koyna, India: a suggestion, *Bull. seism. Soc. Am.,* **73**(2), 679–682.

Gupta, H.K., 1985. The present status of reservoir induced seismicity investigations with special emphasis on Koyna earthquakes, *Tectonophysics,* **118,** 257–279.

Gupta, H.K., Rastogi, B.K. & Narain, H., 1972. Common features of the reservoir associated seismic activities, *Bull. seism. Soc. Am.,* **62,** 481–492.

Hatzfeld, D., Karakostas, V., Ziazia, M., Kassaras, I., Papadimitriou, E., Makropoulos, K., Voulgaris, N. & Papaioannou, C., 2000. Microseismicity and faulting geometry in the Gulf of Corinth (Greece), *Geophys. J. Int.* **141,** 438–456.

Hippolyte, J.C., Angelier, J. & Roure, F., 1994. A major geodynamic change revealed by Quaternary stress patterns in Southern Apennines (Italy), *Tectonophysics,* **230,** 199–210.

HoIton, J., 1999. Four geologic settings dominate oil, gas fields of Italy, Sicily, *Oil Gas J.,* **97,** 81–84.

Hunstad, I., Selvaggi, G., D'Agostino, N., England, P., Clarke, P. & Pierozzi, M., 2003. Geodetic strain in peninsular Italy between 1875 and 2001, *Geophys. Res. Lett.,* **30**(4), 1181, doi:10.1029/2002GL016447.

Improta, L. & Bruno, P.P., 2007. Combining seismic reflection with multifold wideaperture profiling: an effective strategy for high-resolution shallow imaging of active faults, *Geophys. Res. Lett.,* **34,** L20310, doi:10.1029/2007GL031893.

Improta, L., Iannaccone, G., Capuano, P., Zollo, A. & Scandone, P., 2000. Inferences on the upper crustal structure of the Southern Apennines (Italy) from seismic refraction investigations and subsurface data, *Tectonophysics,* **317,** 273–297.

Improta, L., Zollo, A., Herrero, A., Frattini, R., Virieux, J. & Dell'Aversana, P., 2002. Seismic imaging of complex structures by non-linear traveltime inversion of dense wide-angle data: application to a thrust belt, *Geophys. J. Int.,* **151,** 264–278.

Improta, L., Bonagura, M., Capuano, P. & Iannaccone, G., 2003. An integrated geophysical investigations of the upper crust in the epicentral area of the 1980, Ms = 6.9, Irpinia earthquake (Southern Italy), *Tectonophysics,* **361,** 139–169.

Kim, W., Hahm, I.K., Ahn, S.J. & Lim, D.H., 2006. Determining hypocentral parameters for local earthquakes in 1-D using a genetic algorithm, *Geophys. J. Int.,* **166,** 590–600.

Lahr, J.C., 1989. HYPOELLIPSE/version 2.00: a computer program for determining local earthquakes hypocentral parameters, magnitude and first motion pattern, U.S. Geol. Surv Open-File Rep., No. 89–116, 92p.

Maschio, L., Ferranti, L. & Burrato, P., 2005. Active extension in Val d'Agri area, Southern Appenines, Italy: implications for the geometry of seismogenic belt, *Geophys. J. Int.,* **162,** 591–609.

Mazzoli, S. *et al*., 2000. Time and space variability of thin skinned and thick skinned thrust tectonics in the Apennines (Italy), *Rendiconti Lincei Scienze Fisiche e Naturali,* **9,** 5–39.

Mazzotti, A., Stucchi, E., Fradelizio, G.L., Zanzi, L. & Scandone, P., 2000. Seismic exploration in complex terrains: a processing experience in the Southern Apennines, *Geophysics,* **65**(5), 1402–1417.

Menardi Noguera, A. & Rea, G., 2000. Deep structure of the Campanian-Lucanian Arc (Southern Apennine, Italy). *Tectonophysics,* **324,** 239–265.

Ottemoller, L., Nielsen, H.H., Atakan, K., Braunmiller, J. & Havskov, J., 2005. The 7 May 2001 induced seismic event in the Ekofisk oil filed, North Sea, 2005, *J. geophys. Res.,* **110,** doi:10.1029/2004JB003374.

Pantosti, D. & Valensise, G., 1990. Faulting mechanism and complexity of the November 23, 1980 Campania-Lucania earthquake, inferred from surface observations, *J. geophys. Res.,* **95**(15), 15 319–15 341.

Patacca, E., Sartori, R. & Scandone, P., 1990. Tyrrhenian basin and Apenninic arcs: kinematics relations since late Tortonian times. *Mem. Soc. Geol. Ital.,* **45,** 425–451.

Phillips, W.S., Rutledge, J.T., House, L.S. & Fehler, M.C., 2002. Induced micro-earthquake pattern in hydrocarbon and geothermal reservoirs: six case studies, *Pure appl. Geophys.,* **159,** 345–369.

Piccinelli, F.G., Mucciarelli, M., Federici, P. & Albarello, D., 1995. The microseismic network of the Ridracoli Dam, North Italy: data and interpretations, *Pure appl. Geophys.,* **145,** 97–108.

Pino, N.A., Palombo, B., Ventura, G., Perniola, B. & Ferrari, G., 2008. Waveform modelling of historical seismograms of the 1930 Irpinia earthquake provides insight on 'blind' faulting in Southern Apennines (Italy), *J. geophys. Res.,* **113,** B05303, doi:10.1029/2007JB005211.

Pondrelli, S., Morelli, A., Ekstrom, G., Mazza, S., Boschi, E. & Dziewonski, A.M., 2002. European-Mediterranean regional centroid-moment tensor; 1997–2000, *Phys. Earth planet. Inter.,* **130,** 71–101.

Reasenberg, P.A. & Oppenheimer, D., 1985. FPFIT, FPPLOT and FPPAGE: Fortran computer programs for calculating and displaying earthquake fault plane solutions, U.S, Geological Survey Open file report, No 85–739.

Richter, C.F., 1935. An instrumental earthquake magnitude scale, *Bull. seism. Soc. Am.* **25,** 1–32.

Rigo, A., Lyon-Caen, H., Armijo, R., Deschamps, A., Hatzfeld, D., Makropoulos, K., Papadimitriou, P. & Kassaras, I., 1996. A microseismic study in the western part of the Gulf of Corinth (Greece); implications for large-scale normal faulting mechanisms, *Geophys. J. Int.,* **126–3,** 663–688.

Roeloffs, E.A., 1988. Fault stability changes induced beneath a reservoir with cyclic variations in water level, *J. geophys. Res.,* **93,** 2107–2124.

Sambridge M.S. & Gallagher K., 1993. Earthquake hypocenter location using genetic algorithms, *Bull. seism. Soc. Am.,* **83,** 1467–1491.

Scherbaum, F. & Johnson, J., 1992. Programmable interactive toolbox for seismological analysis (PITSA), *IASPEI Software Library,* Vol. 5, Seismological Society of America, El Cerrito.

Shiner, P., Beccaccini A. & Mazzoli, S., 2004. Thin-skinned versus thick-skinned structural models for Apulian carbonate reservoirs: constrains from the Val d'Agri Fileds, S Apennines, Italy, *Mar. Petrol. Geol.,* **21,** 805–827.

Simpson, D.W., Leith, W.S. & Scholz, C.H., 1988. Two types of reservoir-induced seismicity, *Bull. seism. Soc. Am.,* **78,** 2025–2040.

Talebi, S., Nechtschein, S. & Boone, T.J., 1998. Seismicity and casing failures due to steam stimulation in oil sands, *Pure appl. Geophys.,* **153,** 219–233.

Talwani, P., 1997. On the nature of resevoir-induced seismicity, *Pure appl. Geophys.,* **150,** 473–492.

Thurber, C., Roecker, S., Zhang, H., Baher, S. & Ellsworth, W., 2004. Fine-scale structure of the San Andreas fault zone and location of the SAFOD target earthquakes, *Geophys. Res. Lett.,* **31,** doi:10.1029/2003GL019398.

Valensise, G. & Pantosti, D., 2001. The investigation of potential earthquake sources in peninsular Italy: a review, *J. Seism.,* **5,** 287–306.

Waldhauser, F., Ellsworth, W.L. Schaff, D.P. & Cole, A., 2004. Streaks, multiplets, and holes: High-resolution spatiotemporal behavior of Parkfield seismicity, *Geophys. Res. Lett.,* **31,** L18608, doi:10.1029/2004GL020649.

Wallace, R.E., 1984. Patterns and timing of late Quaternary faulting in the Great Basin province and relation to some regional tectonic features, *J. geophys. Res.,* **89,** 5763–5769.

Westaway, R. & Jackson, J., 1987. The earthquake of 1980 November 23 in Campania–Basilicata (southern Italy), *Geophys. J. R. astr. Soc.* **90,** 375–443.

Zoback, M.D. & Zinke, J.C., 2002. Production-induced normal faulting in the Valhall and Ekofish oil fields, *Pure appl. Geophys.,* **159,** 403–420.

APPENDIX: AUTOMATIC *P*-WAVE ARRIVAL TIMES PICKING (MANNEKEN PIX)

We applied a recently developed picking system called 'Manneken-Pix' (hereinafter MPX; Aldersons 2004) based on a single trace approach (Allen 1978, 1982; Baer & Kradolfer 1987), working on each seismogram independently. The main advantage of using an automatic picking system is the reduced time required to examine large data sets to obtain *P*-wave arrival times picking. In addition to the classic picking systems, MPX allows to obtain, for each *P*-wave onset, related polarities and error estimations, the latter based on a weighting engine rigorously calibrated on a reference data set (see Aldersons 2004 and Di Stefano *et al.* 2006 for details). This picking system has been successfully used to analyse local and regional events recorded by the RSNC (Di Stefano *et al.* 2006).

During the calibration process, to accurately set the weighting mechanism, we selected a reference subset of more than 700 vertical-component waveforms from 120 events. The selected waveforms are representative of the entire data set (namely different characteristic frequencies of first arrivals due to different magnitudes, source–receiver distribution and local structure heterogeneities affecting the wave propagation). *P*-wave arrival times were accurately hand-picked, and errors were estimated based on the weighting scheme shown in Table 1. We defined the error boundaries of each class according to the noise level in the waveforms and the sampling rate. This calibration process is intended to make the picking system

Table 4. Performance table of the calibration phase showing the correspondence between MPX (AP) and reference picks (RP) classes.

		AP classes					
		Class 1	Class 2	Class 3	Class 4	Rejected	Total
RP Classes	Class 1	287	71	34	0	2	394
	Class 2	20	76	32	3	1	132
	Class 3	8	19	22	18	2	69
	Class 4	0	5	15	24	5	49
	Rejected	2	2	10	10	35	59

mimic the behaviour of an expert human analyst, trying to predict the same picking uncertainties estimated by the user. Results of the calibration show that MPX was able to locate 107 of the 120 seismic events of the reference data set (corresponding to an efficiency of 89 per cent). MPX attributed 63 per cent of the analysed waveforms to the same class as the human analyst (diagonal elements in Table 4), whereas the leakage toward the off-diagonal elements is small. In particular, the leakage of classes 1 and 2 decreases quickly off-diagonal. This ensures that high-quality picks are not too much downgraded.

To process the data set, we included MPX into a five steps procedure. First, *P* triggers are searched in all the available seismograms to detect rough phase onsets (see light blue line in Fig. A1). For each event, MPX analyses the available triggers, applying an outlier detection algorithm to eliminate blunders and to define a common safety time window, where to look for *P* onsets (Fig. A1). In the second step, MPX tries to pick all seismograms accordingly (MPX Run 1; dashed red line in Fig. A1) and not only the seismograms from the triggered stations. This ensures a very high number of pickings. Then (third step), the procedure yields preliminary 1-D

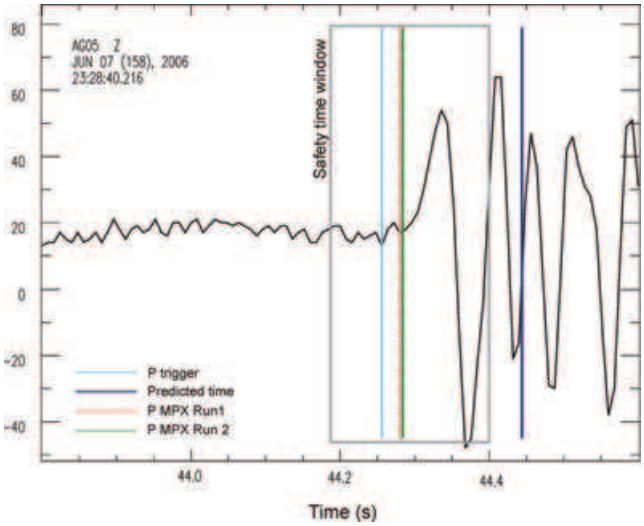

Figure A1. Example of MPX picked waveform. The main steps of the MPX automatic procedure are reported.

event locations by using the Hypoellipse code (Lahr 1989) and calculates predicted arrival times at unpicked stations (violet line in Fig. A1). In the fourth step, MPX searches for accurate *P*-wave onsets in each seismogram (MPX Run2; green line in Fig. A1), taking into account either the reference values from MPX Run 1 or the predicted traveltimes. In the fifth and last step, new locations are produced using the high quality picks of Run 2. In both Run 1 and Run 2, MPX attributes to each pick, an error estimation based on the results of the calibration process.